buildings

MDPI

Article

Study on Mechanical Properties and Damage Characteristics of Fiber-Reinforced Ecological-Matrix-Cemented Aeolian Sand Materials

Danfei Wang [1], Han Yan [2], Chunxiao Qi [2,*], Shasha Lu [3] and Bo Li [4]

[1] Shenyang Polytechnic College, Shenyang 110045, China
[2] China Construction Sixth Bureau Civil Engineering Co., Ltd., Tianjin 300457, China
[3] School of Civil Engineering, Liaoning Technical University, Fuxin 123000, China
[4] China MCC22 Group Corporation Ltd., Tangshan 063000, China
* Correspondence: qcx666666nyx@163.com

Abstract: To improve the quality of trench, backfill projects, this study utilizes solid waste to prepare a controllable low-strength material. Through uniaxial compression, three-point bending tests, and scanning electron microscopy (SEM), the mechanical performance evolution and fiber reinforcement mechanisms of the backfill material are revealed. Based on a two-parameter Weibull distribution probability model, an intrinsic correlation between the number of freeze–thaw cycles, damage variables, and compressive strength is established. The research results indicate that when the NaOH content is 3%, the water-to-solid ratio is 0.4, and the number of freeze–thaw cycles is 0, the sample's mechanical properties reach their local optimum. After curing for 28 days, a significant amount of amorphous gel-like substance is formed inside the system, filling the intergranular spaces between aeolian sand particles, resulting in a relatively dense structure for the backfill material. In response to the degradation caused by the initial defects in the sample, fibers effectively prevent crack initiation. Based on the stochastic characteristics of freeze–thaw damage, the number of freeze–thaw cycles (n) follows the Weibull distribution model well. Using experimental data, evolution equations for the number of freeze–thaw cycles, intrinsic damage, and compressive strength were developed, ultimately establishing the intrinsic relationship between sample damage and strength. The findings provide theoretical support for addressing trench backfill engineering disasters in seasonally frozen regions.

Keywords: aeolian sand; ecological gelation; fiber strengthening; mechanical behavior; damage and deterioration characteristics

check for updates

Academic Editor: Geo Paul

Received: 27 December 2024
Revised: 9 February 2025
Accepted: 16 February 2025
Published: 24 February 2025

Citation: Wang, D.; Yan, H.; Qi, C.; Lu, S.; Li, B. Study on Mechanical Properties and Damage Characteristics of Fiber-Reinforced Ecological-Matrix-Cemented Aeolian Sand Materials. *Buildings* **2025**, *15*, 714. https://doi.org/10.3390/buildings15050714

Copyright: © 2025 by the authors. Licensee MDPI, Basel, Switzerland. This article is an open access article distributed under the terms and conditions of the Creative Commons Attribution (CC BY) license (https://creativecommons.org/licenses/by/4.0/).

1. Introduction

With the advancement of socialist modernization, China has begun to comprehensively strengthen infrastructure construction. Along with the rapid development of urbanization, the number of excavation and backfilling projects such as pipe trench excavation and backfilling in municipal engineering, as well as three backs (bridge abutment back, culvert abutment back, and retaining wall backfilling) in highway engineering, have been increasing year by year. The traditional method of backfilling uses natural graded sand and gravel, which are non-renewable resources. Their over-exploitation has seriously damaged the ecological environment of river channels and mountainous areas. According to statistics, China's annual slag production is about 100 million tonnes [1], and fly ash production is approximately 800 million tonnes [2]. A large amount of solid waste not only piles up,

occupying land area [3], but also endangers public health and ecological safety [4]; China's decertified land area is 257.3713 million square hectares, accounting for 36.81% of the land area [5]. If the abundant reserves of aeolian sand can be used as resources, not only can it solve the problem of a shortage of building materials, but it can also achieve the ecological goal of harmonious coexistence between humans and nature.

Under the environmental protection concept of "green mountains are golden mountains", backfill materials are objectively required to make use of industrial wastes as much as possible, and controlled low-strength material (CLSM) is one of them, in order to realize the inventive use of industrial solid wastes and transform them into treasures. An American Concrete Institute definition of a controlled low-strength material (CLSM) is "a self-compacting, cementitious material primarily used for dense filling" (ACI 299), and this is also known as flowable backfill material, controlled density backfill material, and so on. As a new type of filling material with high fluidity and controllable low strength, CLSM has received a lot of attention from researchers and scholars [6–9]; such raw materials are mostly industrial by-products or wastes, such as slag [10], fly ash [11], red mud [12], gangue [13], steel slag [14], etc., and the commonly used exciters include sodium hydroxide [15], water glass [16], alkali carbonates [17], etc. Compared with silicate cement, geopolymer preparation does not require high-temperature calcination and has significant energy-saving and emission reduction features. Therefore, geopolymer is widely regarded as a green and low-carbon cementitious material, and has increasingly attracted the attention of researchers [18]. Cristelo et al. [19] investigated the effect of calcium content on the effectiveness of alkali-activated materials in improving soft soils by incorporating calcium powder into fly ash-based alkali-activated materials. Sargent et al. [20] used blast furnace slag-based alkali-activated materials for the reinforcement of pulverized sandy soils, and the results showed that the volcanic ash reaction and cementation produced by alkali-activated agents greatly improved the strength and durability of the consolidated soils. Song Di et al. [21] employed red mud, fly ash, and mineral powder as raw materials, NaOH as an exciter, and polycarboxylic acid water-reducing agent as a dispersion to manufacture regulated low-strength materials. They found that the strength development of the materials was closely related to the flocculent, honeycomb, and lamellar structures of the hydration products. Lin Tiangan et al. [22], through SEM and CT tests, found that the polymerized gel generated from solid waste by alkali excitation would have a pore-filling and cementation-enhancing effect on soil, resulting in an increase in the strength of soft soil. Lv Qengfeng et al. [23] investigated the interaction mechanism between clay minerals and alkali-activated materials through microscopic experiments, and the results showed that the cured clay minerals were transformed from loose particles to blocky, dense structures. Rios et al. [24] explored the feasibility of alkali-activated fly ash as a reinforcing material for pulverized soils and showed that the generation of aluminosilicate colloids in consolidated soils is age-dependent [25]. Their strength is related to the formation of aluminosilicate colloids. Gao Yingli et al. [26] investigated the influence of each solid waste interaction on fly ash geopolymer by the response surface method, using calcium carbide slag, desulfurization gypsum, and steel slag admixture as the influencing factors. G. S. Ghataora et al. [27] used fly ash, sand, and cement to prepare fluidized fly ash for the backfilling of pipelines and, by testing them for compressive strength, frost resistance, permanent deformation, and elastic deformation, it was found that they were able to meet the current national quality standards better. Some studies show that [28–30] adding air-entraining agents (AEAs) like resins, synthetic detergents, fatty acid salts, and proteinaceous materials is a standard practice to create a stable air void network in foam concrete for F–T resistance. These agents decrease water surface tension, stabilizing tiny bubbles within the mixture, which serve as

accommodations for ice expansion, cracking prevention, workability enhancement, and segregation reduction [31,32].

The static and dynamic characteristics of soil cured by alkali-activated materials are now the subject of numerous research projects conducted by academics both domestically and globally [6,33–35]. On the other hand, there are less studies on the application of alkali-activated materials for the curing of aeolian sand. The interface between traditional backfill materials and structures often has dead ends, making the quality of filling difficult to ensure. This often leads to roadbed subsidence and other engineering issues. This study developed a controllable low-strength material using slag, fly ash, aeolian sand, and sodium hydroxide through geopolymerization, providing a novel solution for ecological backfill by successfully replacing traditional pipeline trench backfill materials. The mechanical evolution of the material under different conditions was systematically investigated through uniaxial compression and three-point bending tests. Scanning electron microscopy (SEM) was used to elucidate the filling effect of amorphous gel substances and the crack-inhibiting mechanism of fibers, offering microstructural insights for material design. Based on a two-parameter Weibull probability distribution model, a correlation equation was established between freeze–thaw cycles, material damage, and compressive strength, quantitatively describing the material's degradation under freeze–thaw conditions. The findings provide theoretical support for mitigating backfill hazards in seasonally frozen regions and promote the resource utilization of solid waste, contributing to significant environmental benefits.

2. Test Materials and Methods

2.1. Testing Materials

In the preparation process of fiber-reinforced ecological-matrix-cemented aeolian sand material, the aeolian sand was acquired from the Zhang Wu area of Liaoning Province. Natural aeolian sand has a poor gradation, and the particle size is mainly concentrated between 0.63 and 0.92 mm; the inhomogeneity coefficient is Cu3.745, while the curvature coefficient Cc0.821 [36]. Due to the collision and friction between particles caused by wind transport, the angular particles gradually tend to be rounded, and the surface of the particles is smooth. The fly ash was obtained from Rong Changsheng Environmental Protection Material Co., Ltd. (Zhengzhou city, China). The blast furnace slag was purchased from Henan Zhengzhou Yuanheng Environmental Protection Engineering Co., Ltd. (Zhengzhou, China) The chemical composition is indicated in Table 1, and the physical and mechanical characteristics of the slag are reported in Table 2. Polypropylene fiber was purchased from Shandong Shuntong Engineering Materials Co., Ltd. (Ji'nan, China); it is white, translucent, and has a bundled monofilament structure. The basic material was a synthetic fiber known as a polymer hydrocarbon; Table 3 lists its mechanical and physical characteristics. Figure 1 displays the materials that were used for the test.

Table 1. Chemical constituents wt/%.

Chemical Composition	CaO	Fe_2O_3	SiO_2	Al_2O_3	MgO	Na_2O	K_2O	SO_3	FeO	S
Fly ash	4.13	3.77	58.79	25.12	0.45	0.98	1.15	0.39	-	-
Slag	44.36	0.38	33.25	13.27	6.31	0.33	0.28	-	0.89	1.1

Table 2. Physical index parameters of blast furnace slag.

Density g/cm^3	Specific Surface Area m^2/kg	Burning Vector/%	Chlorion/%	Mobility Ratio/%	Water Content/%
2.9	428	0.21	0.024	109	0.32

Table 3. Physical Properties of Polypropylene Fiber.

Type	Density/ ($g \cdot cm^{-3}$)	Tensile Strength/Mpa	Elastic Modulus/Gpa	Melting Point/°C	Ignition Point/°C	Fracture Elongation/%	Dispersibility
Bundle monofilament	0.91	≥300	≥3.5	165	590	≥15	Fabulous



Figure 1. Testing material.

2.2. Test Method

In this paper, the experimental scheme was designed based on 50% airborne sand content, 40% fly ash content, 10% slag content, 9 mm fiber length, and the weight fraction of fiber is 0.5%. This scheme aims to assess the effects of varying NaOH content, different water-to-solid ratios, and various freeze–thaw cycles on the mechanical properties of fiber-reinforced eco-matrix-cemented airborne sand materials, as detailed in Table 4.

Table 4. Test scheme.

Group	Sample Number	NaOH Content	Water–Solid Ratio	Freeze–Thaw Cycles
Group A	S1	1%	0.35	0,3,6,9,12
	S2		0.40	
	S3		0.45	
Group B	S4	2%	0.35	0,3,6,9,12
	S5		0.40	
	S6		0.45	
Group C	S7	3%	0.35	0,3,6,9,12
	S8		0.40	
	S9		0.45	

Fiber-reinforced eco-matrix-cemented materials were prepared using fly ash and slag as cementitious materials and aeolian sand particles as fine aggregates. The specimens were prepared according to the mix ratios in Table 4. According to the specified test ratio, cementitious material, aggregate, alkali activator, and water were weighed out. First, sodium hydroxide and water were mixed in proportion and stirred evenly to ensure complete mixing. Preparing and cooling the alkali activation solution to room temperature prior to use was necessary due to the exothermic dissolution process and the impact of temperature on the test. The two types of cementitious materials were mixed and stirred for 3 min. They were then gradually added to the mixer containing aggregates and fibers and stirred for another 3 min. Subsequently, the prepared alkali activation solution, once cooled, was added and stirred at a uniform speed for 3 min. Both cementitious materials were used at room temperature. Ultimately, the well-blended substance was put into two molds: one round mold, which had a 50 mm diameter and a 100 mm height, and one rectangular mold, which had dimensions of 160 mm by 40 mm by 40 mm. Following the vibrating process, it was left in the curing box for 24 h to remove the mold, and we then put the sample into a standard curing box (the temperature was kept at 20 ± 2 °C and the humidity was kept at about 90%) for 28 days. Figure 2 depicts the particular procedure.



Figure 2. Sample preparation process.

The specimens' mechanical characteristics, such as their flexural strength and 28-day unconfined compressive strength, were assessed using the GB/T 3356-2014 Test Method for Flexural Properties of Oriented Fiber-reinforced Polymer Matrix Composites [37]. Using a WDW-100E microcomputer-controlled electronic universal testing machine (Jinan Ji'nan Times Testing Instrument Co., Ltd., Ji'nan, China), the specimens were tested for unconfined compressive strength and three-point bending integrity. The loading process, depicted in Figures 3 and 4, was controlled at a rate of 0.5 mm/min. The maximum pressure value at specimen failure was recorded. To ensure the reliability of the test data, each test group consisted of three specimens in the same state. The average of the test values from these three specimens was calculated. If the relative standard deviation of the unconfined compressive strength and flexural strength exceeded the permissible difference of 15 percent, the test was to be re-conducted.

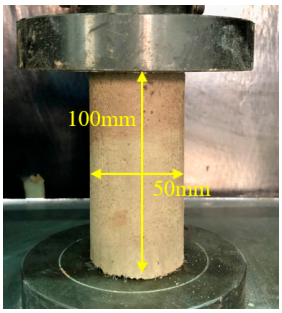


Figure 3. Uniaxial compression test.

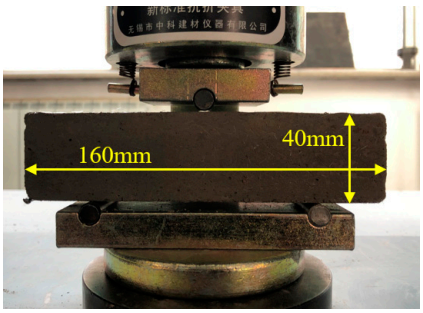


Figure 4. Fracture resistance test.

The specimens are put through freeze–thaw cycles in this test using a quick freeze–thaw testing apparatus. With a precision of one degree Celsius, the apparatus enables accurate temperature control. The specimen center temperature is adjusted to thaw at

+20 °C ± 1 °C and freeze at −20 °C ± 1 °C for this test. Every freeze cycle lasts 24 h and consists of 12 h of freezing and 12 h of melting [36].

Some sample microstructures were observed using a Zeiss MELIN Compact field emission scanning electron microscope (SEM) (Carl Zeiss, Oberkochen, Germany). The damaged sample was picked up and made into a block of approximately 0.5–1 cm^2 area and 0.5–0.8 cm thickness. After drying in the oven at 105 °C, it was fixed on a copper cylindrical table with an approximate height of 1 cm by double-sided adhesive. An appropriate amount of conductive tape was pasted on the fixed section surface. After blowing the debris on the test block surface, it was placed in a vacuum gold-spraying pump to spray gold on its surface. The gold-spraying current was 6–8 mA, and spraying time was 80 s, the working voltage was 20 kV, the beam spot was 1.5–3.5 mm, and the vacuum degree was 2×10^{-3} Pa. Aeolian sand material is cemented into an ecological matrix, and throughout the observation process representative photos are taken and preserved, explaining the occurring state of fiber and revealing the degradation control technology of fiber structure performance.

3. Analysis of Mechanical Properties Test Results

3.1. Test Result

Tests of uniaxial compression were performed under various circumstances on fiber-reinforced ecological-matrix-cemented aeolian sand specimens. The calculation formula of unconfined compressive strength is as follows:

$$q_u = \frac{F}{A} \tag{1}$$

where q_u is the unconfined compressive strength of the sample, Mpa; F is the maximum load when the specimen is destroyed, and N; A is the cross-sectional area of the sample, mm^2.

After calculation, the test results are shown in Table 5.

Table 5. Results of unconfined compression testing of specimens.

Sample Number	28d UCS/Mpa									
	Freeze–Thaw Cycles (0)	CV	Freeze–Thaw Cycles (3)	CV	Freeze–Thaw Cycles (6)	CV	Freeze–Thaw Cycles (9)	CV	Freeze–Thaw Cycles (12)	CV
S1	1.84	0.071	1.57	0.012	1.42	0.103	1.34	0.026	1.26	0.021
S2	2.09	0.042	1.73	0.031	1.55	0.051	1.41	0.015	1.32	0.035
S3	1.76	0.025	1.43	0.026	1.29	0.091	1.21	0.044	1.17	0.115
S4	3.19	0.111	2.82	0.041	2.61	0.035	2.52	0.059	2.45	0.081
S5	3.62	0.056	3.21	0.065	2.99	0.046	2.84	0.011	2.71	0.047
S6	3.04	0.092	2.73	0.105	2.54	0.095	2.41	0.082	2.33	0.031
S7	5.41	0.074	4.94	0.091	4.72	0.088	4.64	0.106	4.59	0.083
S8	5.75	0.124	5.34	0.023	5.09	0.051	4.92	0.004	4.86	0.266
S9	5.13	0.109	4.61	0.044	4.34	0.046	4.22	0.058	4.17	0.054

Samples of fiber-reinforced ecological-matrix-cemented aeolian sand were subjected to three-point bending tests in various settings. According to the basic theory of elastic mechanics, the calculation formula of flexural strength is as follows:

$$f_f = \frac{3FL}{2bh^2} \tag{2}$$

In the formula: f_f is the flexural strength of the sample, Mpa; F is the failure load of the specimen, N; L is the span between supports, mm; b is the width of the sample section, and mm; h is the cross-section height of the sample, mm.

After calculation, the test results are shown in Table 6.

Table 6. Three-point bending test results of specimens.

Sample Number	28d FS/Mpa									
	Freeze–Thaw Cycles (0)	CV	Freeze–Thaw Cycles (3)	CV	Freeze–Thaw Cycles (6)	CV	Freeze–Thaw Cycles (9)	CV	Freeze–Thaw Cycles (12)	CV
S1	0.59	0.007	0.46	0.002	0.35	0.012	0.28	0.003	0.25	0.002
S2	0.73	0.102	0.58	0.061	0.47	0.035	0.42	0.098	0.39	0.011
S3	0.54	0.113	0.37	0.034	0.29	0.006	0.24	0.004	0.22	0.005
S4	1.22	0.064	0.94	0.059	0.79	0.041	0.71	0.019	0.65	0.099
S5	1.35	0.835	1.07	0.084	0.92	0.106	0.85	0.034	0.81	0.064
S6	1.14	0.042	0.83	0.073	0.69	0.045	0.62	0.026	0.57	0.025
S7	1.58	0.079	1.39	0.046	1.26	0.061	1.21	0.109	1.18	0.041
S8	1.69	0.052	1.45	0.085	1.34	0.088	1.27	0.028	1.22	0.068
S9	1.51	0.066	1.29	0.101	1.14	0.125	1.07	0.034	1.03	0.023

3.2. The Effect of Different Factors on the Mechanical Properties of the Sample

The link between the fiber-reinforced ecological-matrix-cemented aeolian sand sample's 28d unconfined compressive strength and the various parameters is determined based on the test findings stated in Table 5, as illustrated in Figure 5. The relationship between the flexural strength of fiber-reinforced ecological-matrix-cemented aeolian sand samples and various parameters is drawn, as illustrated in Figure 6, based on the test findings stated in Table 6.

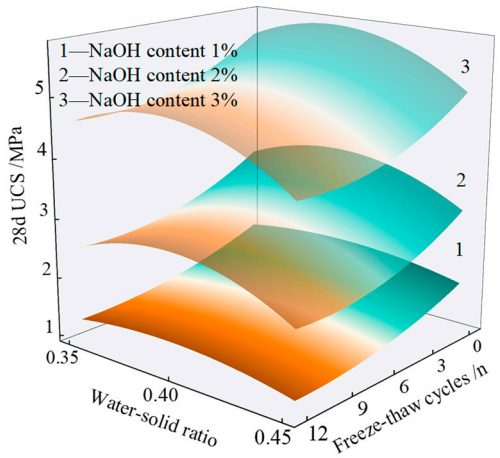


Figure 5. The relationship between the 28d UCS of the specimen and the factors.

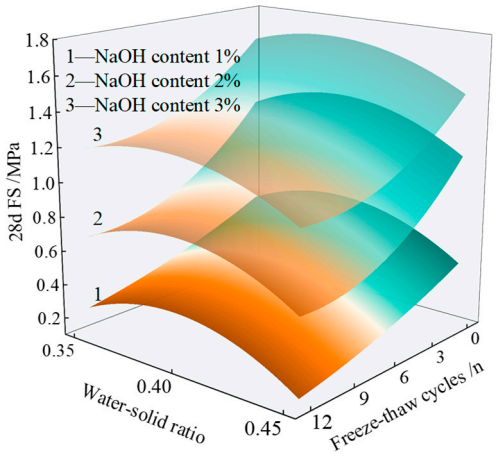


Figure 6. The relationship between the flexural strength of samples and various factors.

It can be observed from Figure 5 that when the NaOH content is 3%, sample S8 reaches maximum compressive strength when the number of freeze–thaw cycles is 0. Under the

same conditions, sample S8's compressive strength increases by 3.66 Mpa compared with that of sample S2 when the NaOH content is 1%. The relationship between the sample flexural strength and the amount of NaOH is shown in Figure 6. Based on the water–solid ratio of the sample of 0.4 and the number of freeze–thaw cycles of 0, when the NaOH amount is 1%, the S2 sample's flexural strength is 0.73 Mpa. When the NaOH amount increases to 3%, the flexural strength of the sample (8) increases to 1.69 Mpa, an increase of 131.51% year-on-year. Combined with Figures 5 and 6, it was identified that, within the scope of this experimental study, with the increase in NaOH content, the compressive and flexural strengths of the sample showed a gradually increasing trend. This is because, when the NaOH content is small, the driving force of the polymerization reaction process is insufficient, and the degree of polymerization of the generated product is small, resulting in a lack of density in the material structure after hardening. With the NaOH content increases, the pH in the polymerization reaction environment increases. This higher pH solution environment promotes the dissolution of Ca, Si, Al, and other elements, such that more gray bodies dissolve to form silicate and aluminate monomers, accelerate the polymerization reaction speed, and increase the reaction intensity, thus generating a more hydraulic cementitious matrix, and the ultimate compressive capacity is Improved [38,39].

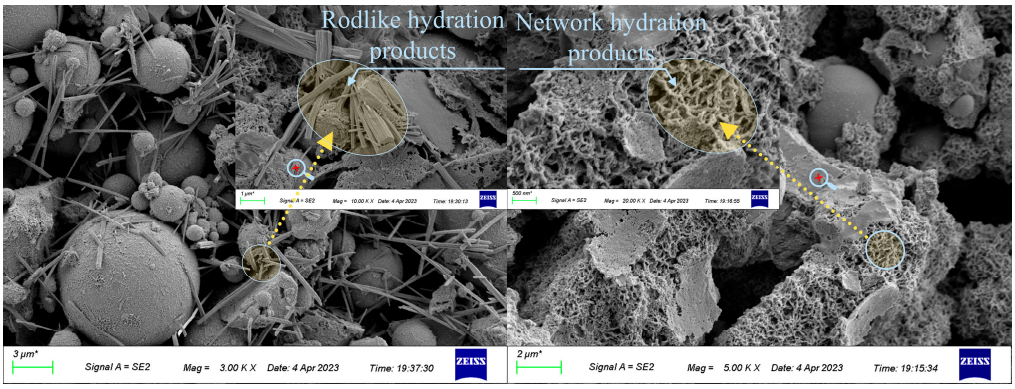
According to Figures 5 and 6, the sample's compressive and flexural strengths tend to rise initially before declining, within the parameters of the experimental investigation, when the water–solid ratio rises. The sample's compressive and flexural strengths reach the local optimum as the water–solid ratio approaches 0.4. NaOH particles are diluted with water to form an alkali solution, and the alkali solution is combined with the cementing material to form slurry, which is wrapped over the surface of aeolian sand particles during mixing. However, the gel substance produced by the synergistic effect of alkali solution and gel material is the main source of cohesion in the blend system. The content of NaOH has an important influence on the mechanical properties of fiber-reinforced, eco-based-gelled aeolian sand. In the process of sample preparation, if the water–solid ratio is small, the water consumption is relatively small, which will lead to a decrease in material fluidity, poor neutralization in the mixing process, insufficient affinity of slurry material, and an inability to effectively wrap aeolian sand particles. During the vibrating process, aeolian sand with a smaller particle size cannot be well filled in the gaps between coarse particles with a larger particle size, resulting in a large number of pores in the backfill material system. When the water–solid ratio is small, the hydration of the ecological matrix is insufficient, which leads to the overall strength of the sample being small. With the increase in the water–binder ratio, the workability of the mixture is improved in the mixing process, and the vibration is more dense after being put into the mold, thus improving the mechanical properties of the sample. When the water–solid ratio exceeds the optimal value because the water consumption is relatively large, bleeding and segregation will occur after mixing, which will affect the molding of the sample. The weakening effect of pores on the strength will gradually become prominent, and the strength of the material will decrease. Therefore, the appropriate water–solid ratio can ensure the hydration reaction is fully carried out, which is beneficial to the strength development of aeolian sand backfill cemented by ecological matrix.

Figures 5 and 6 intuitively reflect the changing trend of backfill sample strength under different conditions with the increase in freeze–thaw cycles. With the increase in freeze–thaw cycles, the internal damage to materials gradually accumulates, and the compressive and flexural strength of fiber-reinforced ecological-matrix-cemented aeolian sand backfill gradually decreases. During the whole freeze–thaw cycle, under the alternating action of positive and negative temperature, the water in the backfill material system changes between solid and liquid, and the water migration caused by the temperature gradient

inside and outside the sample during the freeze–thaw cycle destroys the initial arrangement of aeolian sand particles in the backfill system, changes the position and spacing of aeolian sand particles, and redistributes them. At the same time, under the action of crystallization pressure, the internal structure of the sample is destroyed and the pores are constantly developed, so when the number of freeze–thaw cycles increases from 0 to 6, the mechanical properties of the sample deteriorate obviously, but with the accumulation of freeze–thaw cycles, the damage formed inside the sample tends to be stable, so when the number of freeze–thaw cycles increases from 6 to 12, the strength decay rate of the sample gradually decreases and tends to be flat.

3.3. Microscopic Characterization of Samples

The microstructure of the fiber-reinforced ecological-matrix-cemented aeolian sand backfill was obtained by SEM scanning, and the strength formation mechanism of ecological-cementitious materials was revealed; the influence of the internal microstructure of the samples on the overall macro-properties of the materials was analyzed. Figure 7 shows the micro-morphology of the samples at different ages.



(**a**) Curing period of 3 days (**b**) Curing period of 28 days

Figure 7. Micro-morphology of hydration products (sample S8, number of freeze–thaw cycles is 0).

As can be seen from Figure 7a, when the curing age of the sample is 3 days, spheres (fly ash) are clearly visible in the Figure, and a large number of rod-shaped hydration products coexist. In an alkaline environment, covalent bonds such as aluminum–oxygen bonds and silicon–oxygen bonds in a high-energy state are broken by OH- ions. Free-moving Si monomers $[SiO(OH)_3]^-$ and Al monomers $[Al(OH)_4]^-$ are released from the surface of fly ash and slag, and the dissolved Si and Al monomers continue to self-organize and reconstruct through dehydroxylation. There are three ways to combine these two ion groups, but according to Lowenstein's rule [40], 4-coordinated Al cannot be directly connected, and two $[Al(OH)_4]^-$ cannot undergo a polycondensation reaction. Therefore, the polycondensation reaction of these two ionic groups has only two combinations: two $[SiO(OH)_3]^-$ polycondensation or one $[SiO(OH)_3]^-$ polycondensation combined with one $[Al(OH)_4]^-$ polycondensation. Because this process reduces the concentration of free Si and Al monomers in the system, it further promotes the dissolution of aluminosilicate materials. With the reaction continuing for 28 days, these oligomers further condense to generate a three-dimensional reticulated polysilicate gel composed of $[SiO_4]$ and $[AlO_4]$ tetrahedrons, which gradually coagulate and harden to form a polymer block material, as shown in Figure 7b. This results in a large number of reticulated hydration products, with C-S-H and C-A-S-H becoming closely intertwined. The formation mechanism of the eco-gel matrix is shown in Figure 8, and the EDS spectra of samples at 3 days and 28 days are shown in Figure 9 [41].

$$(Si_2O_5, Al_2O_2)n + 3nH_2O \xrightarrow{\text{NaOH/KOH}} n(OH)_3—Si—O—Al^{(-)}—(OH)_3 \quad (1)$$

$$n(OH)_3—Si—O—Al^{(-)}—(OH)_3 \xrightarrow{\text{NaOH/KOH}} (Na,K)^+—\left(—\underset{\underset{O}{|}}{Si}—O—\underset{\underset{O}{|}}{Al^{(-)}}—O—\right)_n + 3nH_2O \quad (2)$$

$$(Si_2O_5, Al_2O_2)n + 2nSiO_2 + 4nH_2O \xrightarrow{\text{NaOH/KOH}} n(OH)_3—Si—O—\underset{\underset{(OH)_2}{|}}{Al^{(-)}}—O—Si—(OH)_3 \quad (3)$$

$$n(OH)_3—Si—O—\underset{\underset{(OH)_2}{|}}{Al^{(-)}}—O—Si—(OH)_3 \xrightarrow{\text{NaOH/KOH}} (Na,K)^+—\left(—\underset{\underset{O}{|}}{Si}—O—\underset{\underset{O}{|}}{Al^{(-)}}—O—\underset{\underset{O}{|}}{Si}—O—\right)_n + 4nH_2O \quad (4)$$

Figure 8. Formation mechanism of ecological-cementitious matrix.

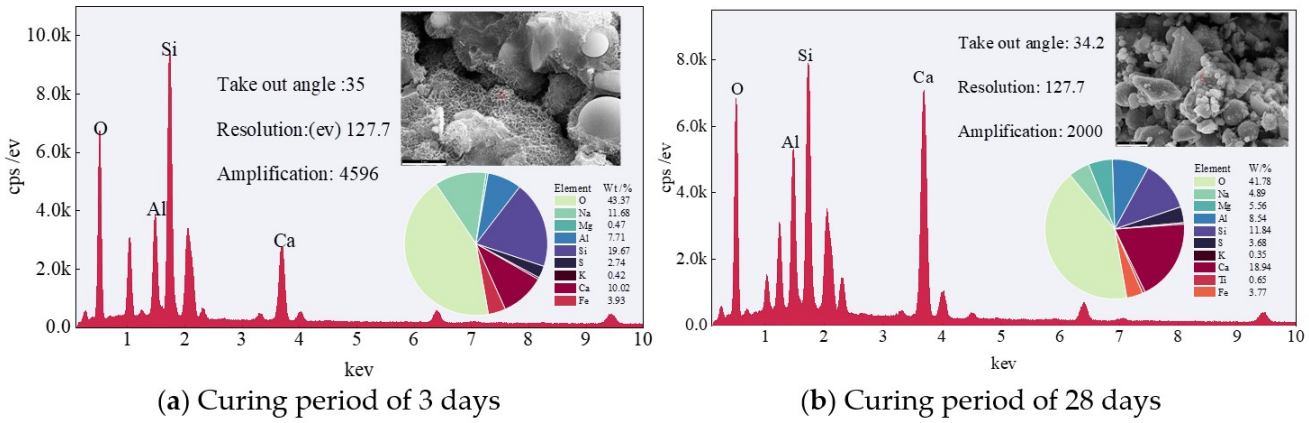
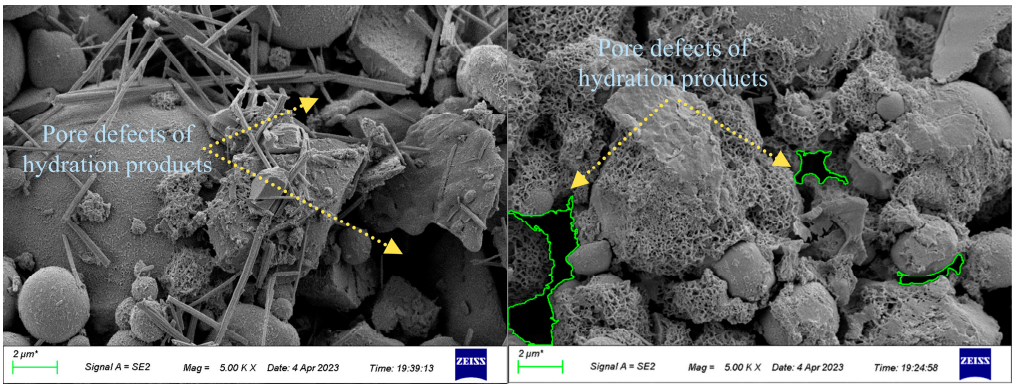


Figure 9. EDS spectrum of sample.

According to the Aim and Goff model theory, when the alkali-activated composite material mixed with superfine admixture is regarded as a multi-component system, there is the most compact packing in the system, and the slag in the backfill is finer than the fly ash. After replacing part of the fly ash, the amorphous slag particles fill the pores between the spherical fly ash particles, which results in the cementitious material having a better gradation and forming a compact packing structure and a meso-level self-compact packing system. As shown in Figure 10a, when the backfill is cured for 3 days, there is a small amount of hydrated calcium silicate (C-S-H) gel and a small amount of hydrated calcium aluminosilicate (C-A-S-H) gel in the particle skeleton of aeolian sand in the system, creating a certain bonding force between the aeolian sand particles. However, a large number of cementitious materials and aeolian sand particles that have not undergone geo-agglomeration accumulate, resulting in obvious voids, and the structure of the backfill material is relatively loose.

When the sample is cured for 28 days, as shown in Figure 10b, a large number of calcium silicate hydrate (C-S-H) gels and calcium aluminosilicate hydrate (C-A-S-H) gels appear in the system. The pore defects are obviously reduced compared with those in the sample cured for 3 days. More gel fills in the pores between the aeolian sand particles, which makes the pores decrease, and the loose structure becomes relatively dense and has better adhesion. Many polymerization products pile up to form a honeycomb network topology structure. This structure, with its multi-wall arrangement and series of continuous honeycomb network structures, can bear external forces from all sides in a decentralized manner. This makes the honeycomb structure highly reliable and stable when resisting external forces and demonstrates excellent geometric properties.



(**a**) Curing period of 3 days (**b**) Curing period of 28 days

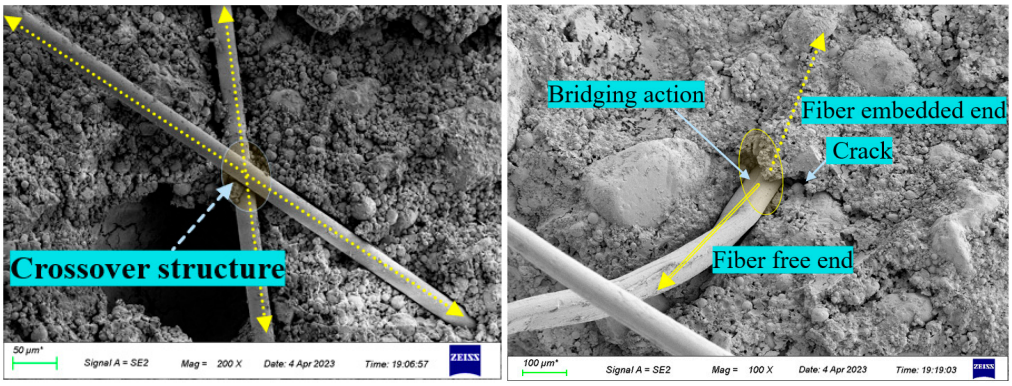
Figure 10. Internal pore defect map of the sample (sample S8, freeze–thaw-cycle number is 0).

The morphological changes in the microcracks and microvoids of the material system have an important influence on its macroscopic mechanical properties. Because the formation of a damage field is essentially a variation in the microscopic structure of the material, the fiber-reinforced ecological-matrix-cemented aeolian sand is a multiphase composite solid containing continuously distributed defects. During the preparation and formation process, defects such as microcracks and microvoids inside the matrix are randomly distributed. During the setting and hardening behavior of the sample, pores are left following the evaporation of pore water, forming an unsaturated area of the polymerization product and resulting in pore defects inside the material (as shown in Figure 10). As an alienated microstructure, the initial defects in the backfill structure generally show a deteriorating trend. When the randomly distributed nano-scale pores of the sample are connected under load, the initial defects or interface cracks develop into microcracks, resulting in microcrack areas and macrocracks, that is, resulting in damage accumulation.

The fiber-reinforced ecological-matrix-cemented aeolian sand backfill is different from the general geopolymer-stabilized aeolian sand material. From a macro perspective, in the mixed matrix, the fiber is small, and the specific surface area is large. When an appropriate amount of fiber is added to the sample, the fibers are evenly distributed inside the matrix, and a three-dimensional network random support system can be formed inside it. As shown in Figure 11a, the fibers act as a spatial network bridge. When the load on the sample is transmitted to the point where the fibers overlap with each other, the cross-lapping point produces relative dislocation under the action of external force, and other interspersed fibers limit the initiation of deformation, thereby dispersing the local stress and forming a three-dimensional space. The stress zone can ideally disperse the external load to other areas inside the sample and reduce the stress concentration inside the sample. This realizes the effect of sharing stress and improves the overall stability.

In early research, Romualdi, Batson, and Mandel proposed the "fiber fracture resistance theory," which explains the constraint on fibers related to the occurrence and development of cracks based on linear elastic fracture mechanics [42,43]. According to the theory of fiber crack resistance, when there are inherent defects in a mixed matrix, and if the aim is to improve the strength, it is necessary to reduce defects as much as possible, improve the toughness of the material (i.e., its ability to resist deformation), and reduce the stress concentration factor at the crack end in the mixed matrix. This theory first assumes that the fiber is evenly distributed in the backfill matrix. If there a tendency of microcrack development in the backfill material matrix, microcracks may form and develop in any direction. Within the average center distance S from the fiber in the backfill matrix, the crack will encounter a fiber that is transverse in front of it. Owing to the existence of this fiber, as shown in Figure 11b, crack propagation is immediately hindered when the crack is

adjacent to the fiber. The crack resistance effect acts throughout, i.e., before and after the specimen is subjected to a force. During stress application, crack propagation is inhibited, and the stress concentration at the crack tip is alleviated. When the combined result of the stress and strain reaches a certain critical value, the crack will expand unstably, that is, the blend aggregate will undergo a steady-state subcritical expansion process after crack initiation and expansion, and then enter the unstable expansion stage until it is destroyed.



(**a**) Fiber occurrence form (**b**) Fiber action form

Figure 11. Mechanism of fiber reinforcement (sample S8, freeze–thaw-cycle number is 0).

Under the action of freeze–thaw cycles, the internal temperature of the ecological-matrix-cemented aeolian sand sample alternates between positive and negative, and the water inside the system experiences a continuous cycle of freezing and flowing. When the internal temperature of the backfill body is lower than zero, the water between the structural pores freezes and the volume expands. At this time, the pore wall experiences the maximum hydrostatic pressure. When the internal temperature of the backfill increases above the freezing temperature, the pore water melts to the liquid state, which is equivalent to a process of hydrostatic pressure unloading. In addition, during the freeze–thaw cycle, there also exists a seepage pressure caused by the infiltration of water from the capillary pores into the gelled pores. Under the effect of the freeze–thaw cycle, the seepage pressure also shows periodic changes. The damage caused by the periodic alternation of loading and unloading is akin to fatigue damage in the material. Therefore, the freeze–thaw-cycle-induced damage to the material can be regarded as a kind of fatigue cumulative damage. However, freeze–thaw-cycle-induced damage has its own characteristics compared to fatigue cumulative damage. Because the internal structure of the material is complex, the distribution of pores and microcracks is highly random, the stress state of the pore wall is very complex, and the internal stress distribution of the sample is uneven under the action of the freeze–thaw cycle. Therefore, freeze–thaw damage can also be regarded as random damage, and is most appropriately understood as random fatigue cumulative damage.

Consider that the freeze–thaw cycle induces random fatigue damage, that is, the influence of the internal pores of the backfill is one of the main factors determining its freeze–thaw resistance. By adding an appropriate amount of polypropylene fiber to the sample, the relatively dense microstructure inside the sample can be loosened to form a microscopic porous structure, so that the pores can withstand a certain frost-heave pressure. On the other hand, owing to the large surface friction coefficient of the polypropylene fiber, the fiber itself can withstand a part of the frost-heave pressure, mitigate the crack propagation caused by the internal stress of the sample, and then reduce the number of crack sources, thereby effectively preventing the diffusion of microcracks caused by the freeze–thaw action inside the sample. This enables the formation of a favorable porous structure inside the material that can also be effectively maintained, along with complete

restriction of the pore spacing. In this pore size range, water cannot easily penetrate adjacent pores; this, in turn, controls the seepage pressure, which allows the microstructure and pore size of the material to meet the frost resistance requirements.

4. Freeze–Thaw Damage Degradation Characteristics of Mixed Matrix

4.1. Freeze–Thaw Damage Characteristics of Mixed Matrix

The freeze–thaw cycle is a process in which the eco-cementitious matrix develops from an unstable state to a stable state. Repeated freeze–thaw cycles change the internal system and external morphology of the sample. To determine the influence of the freeze–thaw cycle on the physical properties of the eco-cementitious aeolian sand sample, the height, volume, and mass of the sample before and after the freeze–thaw are measured, and the test results are shown in Table 7 (taking cylinder sample S8 as an example).

Table 7. Changes in physical indexes of samples corresponding to different freeze–thaw cycles.

Freeze–Thaw Cycles	The Height of the Sample/mm	Volume of the Specimen/mm^3	Quality of Specimen/g
0	97.5	196,249.02	413.65
1	97.75	196,270.75	413.52
2	97.91	196,285.37	413.37
3	98.02	196,297.35	413.19
4	98.17	196,308.59	412.98
5	98.25	196,316.28	412.75
6	98.33	196,322.64	412.41
7	98.39	196,327.52	411.99
8	98.44	196,331.75	411.58
9	98.48	196,334.21	411.08
10	98.51	196,336.29	410.56
11	98.54	196,337.84	409.94
12	98.55	196,339.05	409.18

Based on the test results in Table 7, a plot of the relationship between the physical indexes of the sample and the number of freeze–thaw cycles is shown in Figure 12.

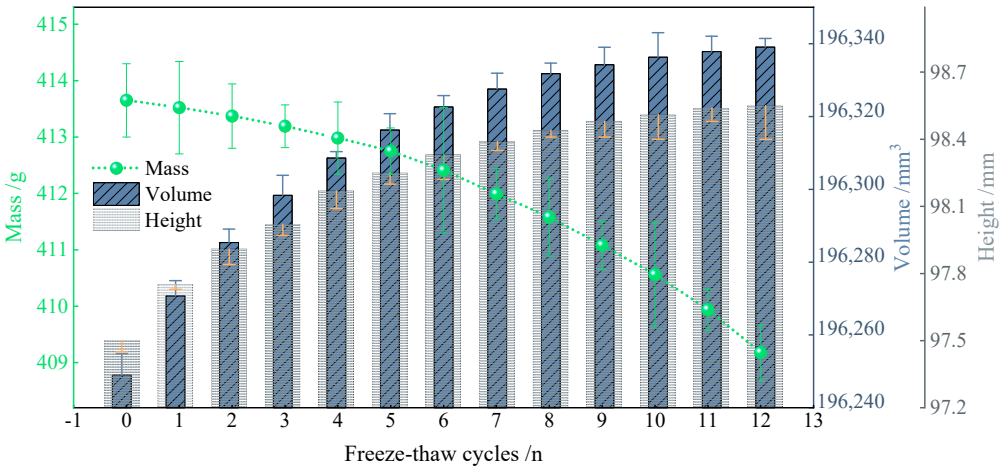


Figure 12. The relationship between the physical indexes of the sample and the number of freeze–thaw cycles.

As can be seen from Figure 12, with the increase in freeze–thaw cycles, the height and volume of the sample gradually increase. When the freeze–thaw cycles exceed six times, the height and volume of the sample remain relatively stable. This indicates that after more than six freeze–thaw cycles, the interior of the sample undergoes significant adjustment and reaches a new balance. With the increase in the number of freeze–thaw

cycles, the internal structure of the sample changes irreversibly, and damage accumulates continuously. From the macroscopic test phenomenon, it can be seen that the surface peeling of the backfill sample occurs throughout the freeze–thaw-cycle process. This phenomenon is characterized by a loss of sample mass, with the mass decreasing gradually as the number of freeze–thaw cycles increases: the more cycles, the faster the mass decreases. This occurs because, during the freeze–thaw cycle, a temperature gradient forms inside and on the surface of the sample, causing moisture within the sample to migrate towards the colder outer surface, where ice crystals then form. The migration of water will cause the surface moisture content of the sample to reach a saturation state. Under the action of negative temperatures, a significant frost-heaving force is initially generated near the outer surface of the sample, which destroys the cement between loose particles in the internal system of the sample. When the temperature rises, the ice crystals near the outer surface of the sample melt first and flow out through pores and cracks, reducing the mass of the sample. From a microscopic perspective, the freeze–thaw cycle causes irreversible expansion of pores in the sample and reduces its strength. With changes in the sample's mass, its mechanical properties also change due to the freeze–thaw cycle. The mass loss rate is introduced here and is calculated using Equation (3).

$$W_n = \frac{G_0 - G_n}{G_0} \times 100\% \tag{3}$$

In the formula, W_n is the mass loss rate of the sample when the number of freeze–thaw cycles is n; G_0 is the initial mass of the sample, and g; G_n is the mass of the sample after n freeze–thaw cycles, g.

According to Formula (3), the mass loss rate of each sample under each number of freeze–thaw cycles is calculated, and the results are shown in Table 8.

Table 8. Sample mass loss rate (%).

Number of Freeze–Thaw Cycles	Rate of Quality-Led Loss								
	S1	**S2**	**S3**	**S4**	**S5**	**S6**	**S7**	**S8**	**S9**
1	0.041	0.026	0.055	0.019	0.021	0.043	0.019	0.031	0.033
2	0.094	0.057	0.127	0.066	0.062	0.102	0.061	0.068	0.084
3	0.148	0.089	0.178	0.124	0.126	0.136	0.115	0.111	0.149
4	0.201	0.195	0.233	0.178	0.194	0.187	0.171	0.162	0.207
5	0.264	0.274	0.291	0.236	0.256	0.245	0.248	0.218	0.275
6	0.356	0.337	0.395	0.301	0.337	0.325	0.336	0.299	0.361
7	0.473	0.426	0.463	0.376	0.431	0.421	0.416	0.401	0.489
8	0.623	0.539	0.551	0.476	0.511	0.503	0.589	0.497	0.612
9	0.731	0.645	0.689	0.581	0.649	0.622	0.732	0.621	0.759
10	0.871	0.792	0.821	0.742	0.805	0.739	0.867	0.747	0.911
11	1.031	0.963	0.985	0.871	1.008	0.906	1.03	0.897	1.083
12	1.218	1.129	1.185	1.057	1.217	1.303	1.233	1.081	1.266

The data in Table 8 show that the relationship between the mass loss rate of the sample and the number of freeze–thaw cycles obeys the power function distribution. The data in the table were fitted and analyzed by Equation (7), and the fitting curve is shown in Figure 13.

$$W_n = an^b \tag{4}$$

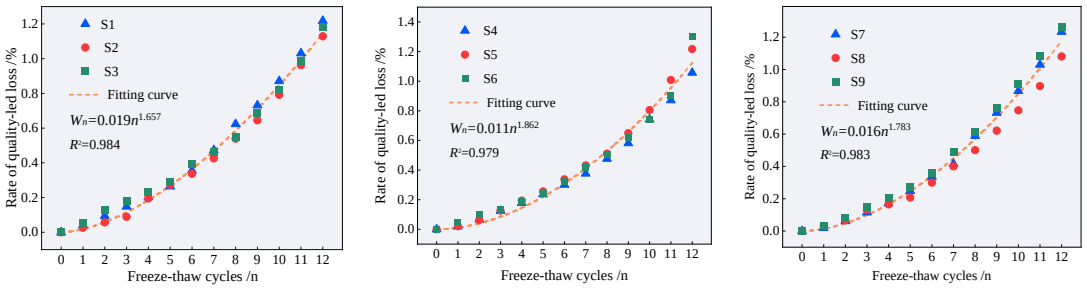
In the formula, n is the number of freeze–thaw cycles and a and b are fitting parameters, dimensionless.

The damage variable describes the damaged state of the material microstructure due to changes in the external environment. The selection principle can reflect some microstructure

characteristics during the material failure process. The physical meaning is precise and convenient for measurement and calculation. The definition of damage is based on the equivalent strain principle:

$$D = 1 - \exp^{-W_n}, \tag{5}$$

where D is the damage variable.



Group A Group B Group C

Figure 13. Fitting curve of relationship between mass loss rate and freeze–thaw cycles.

The fitting equation in Figure 13 is substituted into Equation (5) to obtain the freeze–thaw damage variables of samples in groups A, B, and C, as shown in Equation (6)–(8):

$$D = 1 - e^{-0.019n^{1.657}} \tag{6}$$

$$D = 1 - e^{-0.011n^{1.862}} \tag{7}$$

$$D = 1 - e^{-0.016n^{1.783}} \tag{8}$$

4.2. Freeze–Thaw Damage Model of Mixed Matrix Based on Weibull Distribution

In the process of freeze–thaw damage, the number of freeze–thaw cycles can be regarded as a random variable associated with a certain amount of damage. Due to the anisotropy and inhomogeneity of composites, the failure probability of materials can be expressed, as stated in [44], assuming that both the number of freeze–thaw cycles and the amount of damage follow the Weibull distribution in the composite life prediction model:

$$P = \int_0^n f_{\triangle}(\delta) d\delta \tag{9}$$

where $f_{\triangle}(\delta)$ is the distribution function of the random variable n related to the parameters of the fiber-reinforced ecological-matrix-cemented aeolian sand material.

Damaged-material-failure probability is related to a random variable associated with damage. The failure-probability density function of fiber-reinforced ecological-matrix-cemented aeolian sand material is obtained by Weibull distribution:

$$f(n) = \frac{\beta}{\eta}\left(\frac{n}{\eta}\right)^{\beta-1} \exp\left[-\left(\frac{n}{\eta}\right)^{\beta}\right] \tag{10}$$

where η is the characteristic life parameter and β is the Weibull shape parameter.

Integrating gives the probability cumulative function of the freeze–thaw life N of the corresponding fiber-reinforced ecological-matrix-cemented aeolian sand material:

$$F(N) = 1 - \exp\left[-\left(\frac{N}{\eta}\right)^{\beta}\right] \tag{11}$$

Substituting Equation (10) into Equation (9), the relationship between the material's failure probability and the number of freeze–thaw cycles n is:

$$P(n) = 1 - \exp\left[-\left(\frac{n}{\beta}\right)^{\beta}\right] \tag{12}$$

The failure-probability function of the Weibull distribution function is increasing, and the failure probability increases with the increase in the number of freeze–thaw cycles n. When the number of freeze–thaw cycles of the sample reaches N, the failure probability $P(n) = 1$. Meanwhile, N is the number of freeze–thaw cycles that completely invalidates the fiber-reinforced ecological-matrix-cemented aeolian sand material.

The failure probability and amount of damage in the fiber-reinforced ecological-matrix-cemented aeolian sand material accumulate concurrently with the freeze–thaw-cycle number's increase. Each freeze–thaw cycle will increase the material's failure rate and the damage to the fiber-reinforced ecological-matrix-cemented aeolian sand material. After n freeze–thaw cycles, the damage to the sample is $D(n)$. When the number of freeze–thaw cycles in the sample reaches N, $D(n) = 1$, the material is destroyed, and the failure rate is $P(n)$. After n freeze–thaw cycles, the failure rate of the material is $P(n)$, and the amount of amount of damage in the sample is $D(n)$. Because they conform to the same increasing relationship and follow the same changing characteristics, the damage can be considered equivalent to the failure rate, that is:

$$P(n) = D(n) \tag{13}$$

The freeze–thaw random damage evolution equation based on the Weibull probability distribution is:

$$D(n) = 1 - \exp\left[-\left(\frac{n}{\eta}\right)^{\beta}\right] \tag{14}$$

The Weibull probability distribution model is consistent with the material's actual life characteristics, and the failure probability is consistent with the material's present amount of damage. Therefore, when establishing the freeze–thaw random damage evolution equation, the damage is regarded as the equivalent expression of the material failure rate to establish a random damage equation based on the probability distribution model.

The identical deformation on both sides of Equation (15) can be obtained as follows:

$$\frac{1}{1-D} = \exp\left(\frac{n}{\eta}\right)^{\beta} \tag{15}$$

Consider two logarithms on both sides of the equal sign in Equation (15), respectively, to obtain:

$$\ln\left(\ln\frac{1}{1-D}\right) = \beta\ln\frac{1}{\eta} + \beta\ln(n) \tag{16}$$

Ream $Y = \ln\left(\ln\frac{1}{1-D}\right)$, $X = \ln(n)$, then, Equations (6)–(8) can be written as a first-order linear function:

$$Y = AX + B \tag{17}$$

The maximum likelihood estimation parameters A and B aid the scatter (X_i, Y_i) to achieve the optimal linear state. The parameter estimation data are shown in Table 9.

Table 9. Linear regression parameters of Weibull distribution.

Group	$A(\beta)$	B	η	R^2
Group A	1.377	−3.404	11.846	0.965
Group B	1.479	−3.695	12.162	0.978
Group C	1.518	−3.721	11.601	0.982

The test data points are essentially on a straight line, as shown in Figure 14, and the correlation coefficients are greater than 0.96. Thus, it is feasible to establish the freeze–thaw damage model of fiber-reinforced ecological-matrix-cemented aeolian sand backfill material using the Weibull probability distribution. Subsequently, the damage models of fiber-reinforced ecological-matrix-cemented aeolian sand backfill under freeze–thaw cycles based on the Weibull distribution probability density function of group A, B, and C samples are obtained, as shown in Equations (18)–(20):

$$D(n) = 1 - \exp\left[-\left(\frac{n}{11.846}\right)^{1.377}\right] \tag{18}$$

$$D(n) = 1 - \exp\left[-\left(\frac{n}{12.162}\right)^{1.479}\right] \tag{19}$$

$$D(n) = 1 - \exp\left[-\left(\frac{n}{11.601}\right)^{1.518}\right] \tag{20}$$

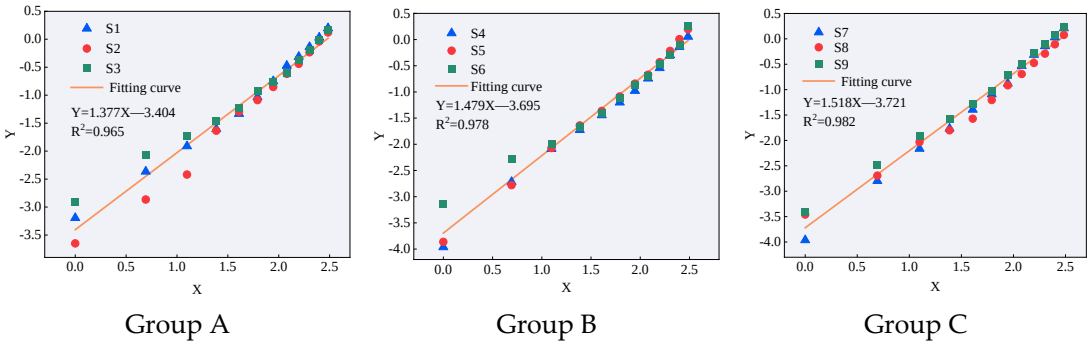


Figure 14. Linear fitting of Weibull distribution.

The relationship between freeze–thaw damage and freeze–thaw cycles of fiber-reinforced ecological-matrix-cemented aeolian sand backfill is determined using the freeze–thaw damage evolution equation provided in Equations (18)–(20), as shown in Figure 15.

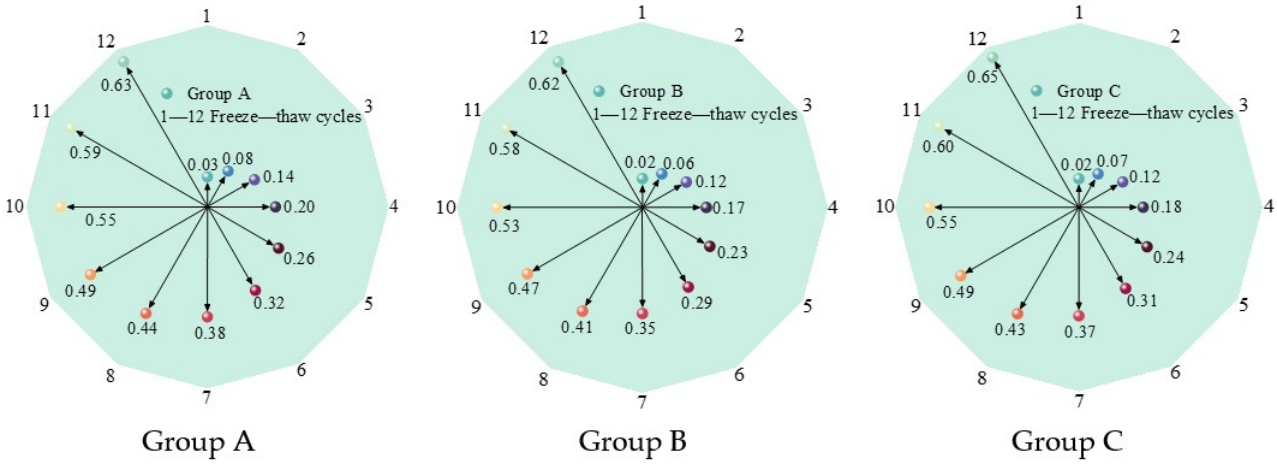


Figure 15. Freeze–thaw damage evolution process diagram.

4.3. Correlation Between Freeze–Thaw Damage and Strength of Mixed Matrix Under Freeze–Thaw Action

Some experimental studies show that the relationship between concrete strength and freeze–thaw cycles obeys the following model [45]:

$$\frac{q_u^D}{q_u} = M \exp\left(\frac{n}{T}\right) \tag{21}$$

However, because the model must satisfy the boundary conditions of $M = 1$ when $n = 0$, the attenuation law between the strength and the number of freeze–thaw cycles cannot be well fitted. Based on the research results of the concrete strength-attenuation model, the model (Equation (21)) is an improvement to the strength-attenuation model of fiber-reinforced ecological-matrix-cemented aeolian sand backfill established by the Weibull distribution probability density function:

$$\frac{q_u^D}{q_u} = \exp\left[-\left(\frac{n}{T}\right)^M\right] \tag{22}$$

where q_u is the sample's compressive strength before freezing and thawing and MPa; n is the number of freeze–thaw cycles. q_u^D is the sample's compressive strength after n freeze–thaw cycles and MPa; M, T is a constant related to material and temperature.

Consider two logarithms on both sides of the equal sign in Equation (22) to obtain:

$$\ln\left[\ln\left(\frac{q_u}{q_u^D}\right)\right] = M \ln n + M \ln\left(\frac{1}{T}\right) \tag{23}$$

Let $\ln\left[\ln\left(\frac{q_u}{q_u^D}\right)\right] = Y$, $\ln n = X$, then, Equation (22) can be written as a first-order linear function:

$$Y = kX + \alpha \tag{24}$$

The samples' compressive strength under different freeze–thaw cycles was incorporated into the relevant model for linear regression and parameter estimation. The material parameters and correlation coefficients are listed in Table 10.

Table 10. Material compressive-strength-related parameters.

Group	α	T	$k(M)$	R^2
Group A	−2.325	51.799	0.589	0.907
Group B	−2.802	94.509	0.616	0.972
Group C	−2.937	313.423	0.511	0.798

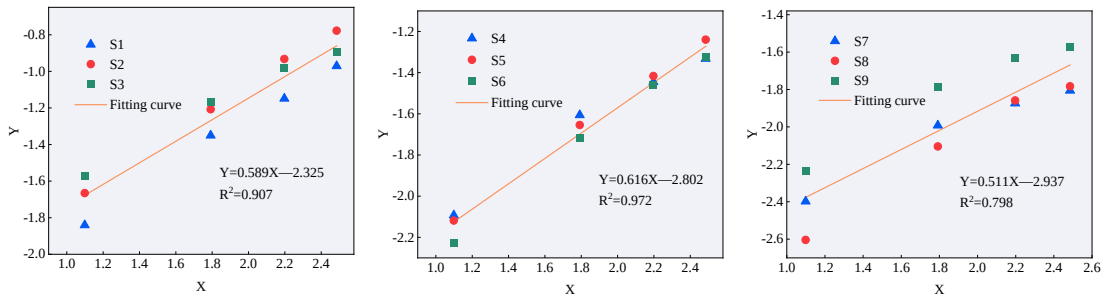
The linear-fitting relationship of the compressive-strength-attenuation law of the sample is shown in Figure 16.

The linear-fitting correlation coefficient R^2 is greater than 0.75, demonstrating that the model incorporates the sample's compressive strength. Through the relevant parameters, the compressive-strength-attenuation model of fiber-reinforced ecological-matrix-cemented aeolian sand under the different conditions in groups A, B, and C are obtained:

$$\frac{q_u^D}{q_u} = \exp\left[-\left(\frac{n}{51.799}\right)^{0.589}\right] \tag{25}$$

$$\frac{q_u^D}{q_u} = \exp\left[-\left(\frac{n}{94.509}\right)^{0.616}\right] \tag{26}$$

$$\frac{q_u^D}{q_u} = \exp\left[-\left(\frac{n}{313.423}\right)^{0.511}\right] \tag{27}$$



Group A Group B Group C

Figure 16. Linear regression diagram of attenuation law of compressive strength of materials.

As the number of freeze–thaw cycles increases, the amount of damage accumulates and strength gradually decays. The freeze–thaw damage model of fiber-reinforced ecological-matrix-cemented aeolian sand has a similar form to the strength-attenuation model under freeze–thaw-cycle conditions, in that there is an internal correlation between the damage and strength of fiber-reinforced ecological-matrix-cemented aeolian sand.

The compressive-strength-attenuation model shown in Equations (25)–(27) is substituted into the freeze–thaw damage evolution equation shown in Equations (18)–(20) after constant deformation, and the relationship between compressive strength and damage is obtained:

$$D(n) = 1 - \exp\left[-7.622\left(\ln\frac{q_u}{q_u^D}\right)^{2.338}\right] \tag{28}$$

$$D(n) = 1 - \exp\left[-20.759\left(\ln\frac{q_u}{q_u^D}\right)^{2.401}\right] \tag{29}$$

$$D(n) = 1 - \exp\left[-149.134\left(\ln\frac{q_u}{q_u^D}\right)^{2.971}\right] \tag{30}$$

The above expression not only shows the relationship between the damage variable and the compressive strength of the aeolian sand material cemented by a fiber-reinforced ecological matrix under freeze–thaw cycles, but it also reflects the influence of the development of micro-defects on its macro-mechanical properties. Simultaneously, changes in the macro-mechanical properties of the material also reflect, to some extent, the evolution process of internal damage.

5. Conclusions

Taking sodium hydroxide content, water–solid ratio, and freeze–thaw cycles as influencing factors, this paper explores the influence of these conditions on the mechanical behavior of fiber-reinforced ecological-matrix-cemented aeolian sand materials. It reveals the fiber-ductility-strengthening mechanism with the help of micro-electron microscope scanning equipment and expounds on the damage evolution characteristics of the samples based on mass loss rate, thereby drawing the following conclusions:

(1) The compressive strength and flexural strength of the specimens increased with the addition of NaOH content, and exhibited a trend of initially increasing and then de-creasing as the water-to-solid ratio increased. When the NaOH content was 3%, the water-to-solid ratio was 0.4, and the number of freeze–thaw cycles was 0, the mechanical properties of the fiber-reinforced ecological-matrix-cemented aeolian sand material reached a local optimum.

(2) As the number of freeze–thaw cycles increased from 0 to 6, the mechanical properties of the specimens showed significant degradation. However, with the accumulation of freeze–thaw cycles, the internal damage in the specimens gradually stabilized. When the number of freeze–thaw cycles increased from 6 to 12, the rate of strength deterioration slowed down and eventually leveled off.

(3) A suitable amount of fiber forms a three-dimensional network support system within the material, effectively preventing the relative displacement of aeolian sand particles. This system generates a crack-blocking effect in the ecological-cemented aeolian sand matrix, suppressing the structural degradation caused by initial defects within the system, thereby significantly improving the overall stability of the specimens.

(4) The number of freeze–thaw cycles (n) follows the Weibull distribution well, and the damage model obtained from the experimental data fitting demonstrates high accuracy (with correlation coefficients greater than 0.95). This study establishes a relationship expression between the compressive strength of the specimens and the number of freeze–thaw cycles, providing a scientific basis for subsequent material optimization and practical applications.

Author Contributions: Methodology, D.W.; Formal analysis, S.L.; Investigation, B.L.; Data curation, S.L.; Writing—original draft, D.W. and S.L.; Writing—review & editing, H.Y., C.Q. and B.L.; Funding acquisition, H.Y. and C.Q. All authors have read and agreed to the published version of the manuscript.

Funding: This research received no external funding.

Data Availability Statement: The datasets generated or analyzed during this study are available from the corresponding author on reasonable request.

Conflicts of Interest: Author Han Yan and Chunxiao Qi were employed by the company China Construction Sixth Bureau Civil Engineering Co., Ltd. Author Bo Li was employed by the company China MCC22 Group Corporation Ltd. The remaining authors declare that the research was conducted in the absence of any commercial or financial relationships that could be construed as a potential conflict of interest.

References

1. Tripathy, S.K.; Dasu, J.; Murthy, Y.R.; Kapure, G.; Pal, A.R.; O Filippov, L. Utilisation perspective on water quenched and air-cooled blast furnace slags. *J. Clean. Prod.* **2020**, *262*, 121354. [CrossRef]
2. Zhao, X.-Y.; Yang, J.-Y.; Ning, N.; Yang, Z.-S. Chemical stabilization of heavy metals in municipal solid waste incineration fly ash: A review. *Environ. Sci. Pollut. Res.* **2022**, *29*, 40384–40402. [CrossRef]
3. Yang, T.; Yao, X.; Zhang, Z.; Wang, H. Mechanical property and structure of alkali-activated fly ash and slag blends. *J. Sustain. Cem. Based Mater.* **2012**, *1*, 167–178. [CrossRef]
4. Shekhawat, P.; Sharma, G.; Singh, R.M. Morphology, and microstructure of waste material-based geopolymer with flyash, eggshell powder, and soft soil. *Mater. Lett.* **2023**, *334*, 133621. [CrossRef]
5. Zan, G.; Wang, C.; Li, F.; Liu, Z.; Sun, T. Main results and analysis of the sixth national desertification and desertification survey. *For. Resour. Manag.* **2023**, *1*, 1–7. [CrossRef]
6. Zhu, Y.; Liu, D.; Fang, G.; Wang, H.; Cheng, D. Utilization of excavated loess and gravel soil in controlled low strength material: Laboratory and field tests. *Constr. Build. Mater.* **2022**, *360*, 129604. [CrossRef]
7. Wang, L.; Feng, W.; Lazaro, S.A.M.; Li, X.; Cheng, Y.; Wang, Z. Engineering properties of soil-based controlled low-strength materials made from local red mud and silty soil. *Constr. Build. Mater.* **2022**, *358*, 129453. [CrossRef]
8. Dueramae, S.; Sanboonsiri, S.; Suntadyon, T.; Aoudta, B.; Tangchirapat, W.; Jongpradist, P.; Pulngern, T.; Jitsangiam, P.; Jaturapitakkul, C. Properties of lightweight alkali activated controlled Low-Strength material using calcium carbide residue–Fly ash mixture and containing EPS beads. *Constr. Build. Mater.* **2021**, *297*, 123769. [CrossRef]
9. Bencardino, F.; Mazzuca, P.; Carmo, R.D.; Costa, H.; Curto, R. Cement-Based Mortars with Waste Paper Sludge-Derived Cellulose Fibers for Building Applications. *Fibers* **2024**, *12*, 13. [CrossRef]
10. Lachemi, M.; Şahmaran, M.; Hossain, K.M.A.; Lotfy, A.; Shehata, M. Properties of controlled low-strength materials incorporating cement kiln dust and slag. *Cem. Concr. Compos.* **2010**, *32*, 623–629. [CrossRef]

11. Gupt, C.B.; Bordoloi, S.; Sekharan, S. Contaminant retention affected by controlled and uncontrolled pH for fly ash-bentonite composites used as landfill liner material. *J. Clean. Prod.* **2023**, *406*, 136924. [CrossRef]
12. Wang, C.; Li, Z.; Zhou, Z.; Gao, Y.; Zhang, J. Compatibility of different fibres with red mud-based geopolymer grouts. *Constr. Build. Mater.* **2022**, *315*, 125742. [CrossRef]
13. Li, M.; Peng, Y.; Zhang, J.; Zhao, Y.; Wang, Z.; Guo, Q.; Guo, S. Properties of a backfill material prepared by cementing coal gangue and fly ash through microbial-induced calcite precipitation. *Constr. Build. Mater.* **2023**, *384*, 131329. [CrossRef]
14. Rui, Y.; Rui, Y.; Qian, C.; Qian, C.; Zhang, X.; Zhang, X.; Ma, Z.; Ma, Z. Different carbon treatments for steel slag powder and their subsequent effects on properties of cement-based materials. *J. Clean. Prod.* **2022**, *362*, 132407. [CrossRef]
15. Su, Y.; Qiu, H.; He, X.; Yang, J.; Wang, Y.; Zeng, S.; Strnadel, B. Structural Analysis of Hydration Products of Ultrafine Fly Ash Activated by Weak Alkali. *Mater. Bull.* **2019**, *33*, 2376–2380. [CrossRef]
16. Ding, Z.; Su, Q.; Bian, H.; Wang, Q.; Zhou, J. Effect of water glass modulus on mechanical properties of geopolymer recycled concrete. *J. Build. Mater.* **2023**, *26*, 61–70. [CrossRef]
17. Liu, Y.; Shi, C.; Zhang, Z.; Li, N. An overview on the reuse of waste glasses in alkali-activated materials. *Resour. Conserv. Recycl.* **2019**, *144*, 297–309. [CrossRef]
18. Shi, C.; Qu, B.; Provis, J.L. Recent progress in low-carbon binders. *Cem. Concr. Res.* **2019**, *122*, 227–250. [CrossRef]
19. Cristelo, N.; Glendinning, S.; Fernandes, L.; Pinto, A.T. Effect of calcium content on soil stabilisation with alkaline activation. *Constr. Build. Mater.* **2012**, *29*, 167–174. [CrossRef]
20. Sargent, P.; Hughes, P.N.; Rouainia, M.; White, M.L. The use of alkali activated waste binders in enhancing the mechanical properties and durability of soft alluvial soils. *Eng. Geol.* **2013**, *152*, 96–108. [CrossRef]
21. Song, D.; Pang, L.; Yang, D.; Lu, M.; Zhao, Y.; Chen, R. Preparation and properties of alkali-activated red mud-based controllable low-strength materials. *Met. Mine* **2022**, 238–243. [CrossRef]
22. Lin, T.; He, H.; Xu, D.; Zhou, Z.; Yao, J. Study on mechanical properties and microscopic test of soft soil reinforced by geopolymer. *J. Yangtze River Acad. Sci.* **2018**, *35*, 104–108. [CrossRef]
23. Lv, Q.; He, J.; Wang, Z.; Yu, J.; Li, C. Interaction mechanism between clay minerals and alkali-activated geopolymers. *J. Eng. Geol.* **2020**, *28*, 1205–1212. [CrossRef]
24. Rios, S.; Cristelo, N.; da Fonseca, A.V.; Ferreira, C. Structural performance of alkali-activated soil ash versus soil cement. *J. Mater. Civ. Eng.* **2016**, *28*, 04015125. [CrossRef]
25. Chen, R.; Zhu, Y.; Lai, H.P.; Bao, W. Stabilization of soft soil using low-carbon alkali-activated binder. *Environ. Earth Sci.* **2020**, *79*, 1–13. [CrossRef]
26. Gao, Y.; Zhu, Z.; Meng, H.; Hu, S.; Li, Z. Synergistic enhancement mechanism of carbide slag-desulfurization gypsum-steel slag modified geopolymer. *J. Build. Mater.* **2023**, *26*, 870–878. [CrossRef]
27. Ghataora, G.S.; Alobaidi, I.M.; Billam, J. Use of pulverized fuel ash in trench backfill. *J. Mater. Civ. Eng.* **2000**, *12*, 228–237. [CrossRef]
28. Zhang, B.; Li, Q.; Niu, X.; Yang, L.; Hu, Y.; Zhang, J. Influence of a novel hydrophobic agent on freeze-thaw resistance and microstructure of concrete. *Constr. Build. Mater.* **2021**, *269*, 121294. [CrossRef]
29. Zuo, S.; Yuan, Q.; Huang, T.; Wang, Z.; Zhang, K.; Liu, J. Rheology and air entrainment of fresh Portland cement mortars in simulated low air pressure environments. *Cem. Concr. Compos.* **2023**, *135*, 104848. [CrossRef]
30. Shah, H.A.; Yuan, Q.; Zuo, S. Air entrainment in fresh concrete and its effects on hardened concrete-a review. *Constr. Build. Mater.* **2021**, *274*, 121835. [CrossRef]
31. Zhang, B. Durability of low-carbon geopolymer concrete: A critical review. *Sustain. Mater. Technol.* **2024**, *40*, e00882. [CrossRef]
32. Zhang, B.; Zhu, H.; You, C.; Yang, Z.; Liu, J.; Peng, H. Flexural durability of BFRP bars reinforced geopolymer-based coral aggregate concrete beams conditioned in marine environments. *J. Build. Eng.* **2024**, *15*, 109959. [CrossRef]
33. Chen, R.; Congress, S.S.C.; Cai, G.; Duan, W.; Liu, S. Sustainable utilization of biomass waste-rice husk ash as a new solidified material of soil in geotechnical engineering: A review. *Constr. Build. Mater.* **2021**, *292*, 123219. [CrossRef]
34. Qin, Z.; Jin, J.; Liu, L.; Zhang, Y.; Du, Y.; Yang, Y.; Zuo, S. Reuse of soil-like material solidified by a biomass fly ash-based binder as engineering backfill material and its performance evaluation. *J. Clean. Prod.* **2023**, *402*, 136824. [CrossRef]
35. Yu, Q.; Nagataki, S.; Lin, J.; Saeki, T.; Hisada, M. The leachability of heavy metals in hardened fly ash cement and cement-solidified fly ash. *Cem. Concr. Res.* **2005**, *35*, 1056–1063. [CrossRef]
36. Zhang, X.; Pang, S.; Geng, J.; Wang, Q.; Su, L.; Han, J.; Tian, L. Study on shear resistance and crack resistance and toughening mechanism of fiber reinforced cement stabilized aeolian sand. *Theor. Appl. Fract. Mech.* **2023**, *123*, 103700. [CrossRef]
37. *GB/T 3356-2014.07-24*; National Aircraft Standardization Technical Committee (SAC/TC 435) "Test Method for Flexural Properties of Oriented Fiber Reinforced Polymer Matrix Composites". National Technical Committee for Standardization of Fiber Reinforced Plastics: Beijing, China, 2014.
38. Yin, H.; Liu, J.; Zhou, X.; Qi, H.; Liu, S.; Pang, S. Flexural properties of fiber-reinforced alkali slag-red mud geopolymer. *Constr. Build. Mater.* **2023**, *370*, 130708. [CrossRef]

39. Pang, S.; Zhang, X.; Zhu, K.; Li, J.; Su, L. Study on mechanical properties and micro characterization of fibre reinforced ecological cementitious coal gangue materials. *Polymers* **2023**, *15*, 700. [CrossRef]
40. Duan, J.; Li, J.; Lu, Z.; Liao, Q. First-principles study of polycondensation reaction of geopolymer cementitious materials. *Artif. Crystallogr.* **2014**, *43*, 2416–2423. [CrossRef]
41. Zhang, D.; Wang, A. summary of research on properties and engineering application of geopolymer cementitious materials. *J. Build. Sci. Eng.* **2020**, *37*, 13–38. [CrossRef]
42. Wecharatana, M.; Shah, S.P. A model for predicting fracture resistance of fiber reinforced concrete. *Cem. Concr. Res.* **1983**, *13*, 819–829. [CrossRef]
43. Pang, S.; Li, J.; Xie, F.; Wang, G.; Fan, H.; Zhu, K. Research on improving the flexural performance of alkali-activated geopolymer cemented coal gangue through layered addition of fibers. *J. Build. Eng.* **2024**, *96*, 110549. [CrossRef]
44. Yan, J.; Zou, C. Life assessment method of concrete materials under freeze-thaw cycles. *J. Harbin Inst. Technol.* **2011**, *43*, 11–15. [CrossRef]
45. Qian, C.; Stroeven, P. Fracture properties of concrete reinforced with steel–polypropylene hybrid fibres. *Cem. Concr. Compos.* **2000**, *22*, 343–351. [CrossRef]

Disclaimer/Publisher's Note: The statements, opinions and data contained in all publications are solely those of the individual author(s) and contributor(s) and not of MDPI and/or the editor(s). MDPI and/or the editor(s) disclaim responsibility for any injury to people or property resulting from any ideas, methods, instructions or products referred to in the content.